PAPER

Check for updates

Can surface reactivity of mixed crystals be predicted from their counterparts? A case study of $(Bi_{1-x}Sb_x)_2Te_3$ topological insulators†

Andrey A. Volykhov, [ab] Jaime Sánchez-Barriga, [c] Maria Batuk, [d]
Carolien Callaert, [d] Joke Hadermann, [d] Anna P. Sirotina, [ae] Vera S. Neudachina, [a]
Alina I. Belova, [a] Nadezhda V. Vladimirova, [a] Marina E. Tamm, [a]
Nikolay O. Khmelevsky, [f] Carlos Escudero, [g] Virginia Pérez-Dieste, [g]
Axel Knop-Gericke [h] and Lada V. Yashina *[a]

The behavior of ternary mixed crystals or solid solutions and its correlation with the properties of their binary constituents is of fundamental interest. Due to their unique potential for application in future information technology, mixed crystals of topological insulators with the spin-locked, gapless states on their surfaces attract huge attention of physicists, chemists and material scientists. $(Bi_{1-x}Sb_x)_2Te_3$ solid solutions are among the best candidates for spintronic applications since the bulk carrier concentration can be tuned by varying x to obtain truly bulk-insulating samples, where the topological surface states largely contribute to the transport and the realization of the surface quantum Hall effect. As this ternary compound will be evidently used in the form of thin-film devices its chemical stability is an important practical issue. Based on the atomic resolution HAADF-TEM and EDX data together with the XPS results obtained both *ex situ* and *in situ*, we propose an atomistic picture of the mixed crystal reactivity compared to that of its binary constituents. We find that the surface reactivity is determined by the probability of oxygen attack on the Te–Sb bonds, which is directly proportional to the number of Te atoms bonded to at least one Sb atom. The oxidation mechanism includes formation of an amorphous antimony oxide at the very surface due to Sb diffusion from the first two quintuple layers, electron tunneling from the Fermi level of the crystal to oxygen, oxygen ion diffusion to the crystal, and finally, slow Te oxidation to the +4 oxidation state. The oxide layer thickness is limited by the electron transport, and the overall process resembles the Cabrera–Mott mechanism in metals. These observations are critical not only for current understanding of the chemical reactivity of complex crystals, but also to improve the performance of future spintronic devices based on topological materials.

*[a] Lomonosov Moscow State University, Leninskie Gory 1/3, 119991 Moscow, Russia.
E-mail: yashina@inorg.chem.msu*

*[b] Institute of General and Inorganic Chemistry RAS, Leninsky Avenue 31,
119991 Moscow, Russia*

*[c] Helmholtz-Zentrum Berlin für Materialien und Energie, Elektronenspeicherring
BESSY II, Albert-Einstein-Strasse 15, 12489 Berlin, Germany*

*[d] EMAT, Department of Physics, University of Antwerp, Groenenborgerlaan 171,
2020 Antwerp, Belgium*

*[e] Institute of Nanotechnology of Microelectronics RAS, Nagatinskaya str., 16A/11,
115487 Moscow, Russia*

*[f] Moscow State University of Technology "STANKIN", Vadkovsky side-street 1,
127994 Moscow, Russia*

*[g] ALBA Synchrotron Light Source, Carrer de la Llum 2-26,
08290 Cerdanyola del Vallès, Barcelona, Spain*

*[h] Department of Inorganic Chemistry, Fritz-Haber-Institut der
Max-Planck-Gesellschaft, Faradayweg 4-6, 14195 Berlin, Germany*

† Electronic supplementary information (ESI) available: Crystal growth and characterisation, atomic scale composition characterisation of bulk crystals, oxide layer and subsurface layer structure, reactivity descriptor, oxide layer thickness calculation, oxidation kinetics measured *in situ*. See DOI: 10.1039/c8tc02235f

Introduction

Surface reactivity of inorganic crystals revealed in solid–gas reactions is a function of many factors, such as crystal structure, quantity of point defects, density of linear, planar and volume defects, crystal purity *etc.*, with the composition being the most important parameter. Within the same class of binary materials, the trends in reactivity are already established: the reactivity is higher for compounds composed of lighter cations and heavier anions,[1–6] with the main factor being the higher energy benefit for oxygen to form specific bonds. However, a question remains open: can the overall reactivity of mixed crystals $(A_{1-x}B_x)C$, both solid solutions and ordered phases, be predicted from the behavior of their constituents? On the one hand, for solid solutions a gradual change in reactivity from the typical value of AC to that of BC is anticipated, with the more reactive

component playing the major role in reactivity. It can be explained by the formation of oxygen bonds with the more reactive component and its surface segregation.[7] On the other hand, for dilute solid solutions the local environment of the impurity atoms B is formed by the foreign lattice AC, which can potentially make the B atoms vulnerable to a chemical attack. To the best of our knowledge, there is no theoretical basis or phenomenological approach to describe the reactivity of mixed crystals from the properties of their counterparts as a function of their composition.

Generally, solid solutions are attractive in many fields since their properties can be smoothly tuned by varying the composition. This is widely used for fine adjustment of electronic, magnetic, mechanic and many other material properties, for instance, to control precisely both the optical band gap and the lattice constant (or mismatch) in light-emitting diodes (LEDs), or to realize topological p–n junctions through compositionally graded doping for spintronics. In this context, mixed crystals of topological insulators are of special interest. While gapped in the bulk due to the strong spin–orbit coupling, topological insulators are characterized by spin-locked gapless states occurring at their surfaces or interfaces with trivial insulators, *i.e.* the so-called topological surface states (TSSs).[8–15] However, one of the major challenges for the utilization of topological insulators in the future information technology is the suppression of their residual bulk conductance, which outbalances the surface contribution. Therefore, to disentangle the contribution from TSSs in emergent transport phenomena, and, consequently, for device applications, it is necessary to place the Fermi level (FL) within the bulk energy gap. Conversely, the most studied topological insulators including Bi_2Se_3, Bi_2Te_3 and Sb_2Te_3 are degenerated semiconductors that exhibit metallic conductivity dominated by bulk carriers originating from the native defects and nonstoichiometry.[16,17]

Many efforts to shift the Fermi level inside the bulk band gap by electron or hole doping.[18–21] Only in few of such experiments, however, the contribution from the TSS has been clearly observed in the transport measurements,[20] thus leading to the realization of the surface quantum Hall effect.[13] Nevertheless, full control of the surface-dominated transport in topological insulator systems is still a challenge. The simplest quasibinary system to meet these requirements is naturally Bi_2Se_3–Sb_2Te_3,[22] where the Fermi level can cross the Dirac point. This condition, however, can be also realized for the $(Bi_{1-x}Sb_x)_2Te_3$ solid solutions if we use the chalcogen-rich side to get the n-type conductivity for Bi_2Te_3 and for $Bi_2(Se_{1-x}Te_x)_3$ if the p-type Bi-rich Bi_2Te_3 is a counterpart.[23] Recently, large bulk resistivity values were reached for a Bi-based ternary compound, Bi_2Te_2Se.[24] Clear signatures of the helical surface states were observed, including the spin polarization found by spin-resolved angle-resolved photoemission spectroscopy (SR-ARPES),[25] the non-trivial Berry phase in quantum oscillations,[24] and unique scattering properties of electrons observed by scanning tunneling microscopy (STM).[23,26]

For $(Bi_{1-x}Sb_x)_2Te_3$ the TSSs exist over the entire range of x with the reduction of the bulk carrier density near the truly bulk-insulating state occurring for certain intermediate composition.[27]

This fact renders $(Bi_{1-x}Sb_x)_2Te_3$ solid solution one of the most important candidate materials to be used in the form of thin films for future applications, its stability during preparation and device operation is an important practical issue. Therefore, here we choose this system to systematically investigate the fundamental question regarding the reactivity of mixed crystals towards oxygen and its correlation with the reactivity of their constituents, less reactive Bi_2Te_3 and more reactive Sb_2Te_3, using a multi-technique approach that probes chemical reactions at the atomic scale.

Results and discussion

Surface *vs.* bulk properties

The electronic band structure of the $(Bi_{1-x}Sb_x)_2Te_3$ crystals near the Γ point of the surface Brillouin zone is displayed in Fig. 1a–e. In detail, we observe intensity contributions from the TSS, bulk-conduction and valence band states and a progressive upward shift of the Dirac point which is in line with the previous experimental and theoretical findings.[22,27] For x = 0 (*i.e.* Bi_2Te_3) the Fermi level is located in the bulk-conduction band, while for x = 0.55 it is already inside the bulk band gap. At x = 0.8 the Fermi level is very close to the Dirac point, and beyond this composition the crystals become strongly p-doped. At the extreme x = 1 the TSS is entirely located above the Fermi level (Fig. 1f). In addition, we clearly observe how the position of the TSS relative to the bulk valence and conduction bands changes evenly from Bi_2Te_3, for which the Dirac point is buried in the bulk-valence band, to Sb_2Te_3, where the Dirac point is above the middle of the gap, with the corresponding upward shift reaching ~ 400 meV (see Fig. 1g and h). This is accompanied by an increase in group velocity of Dirac fermions within the TSS from 3.1×10^{-5} m s^{-1} to 5×10^{-5} m s^{-1} (Fig. 1i).

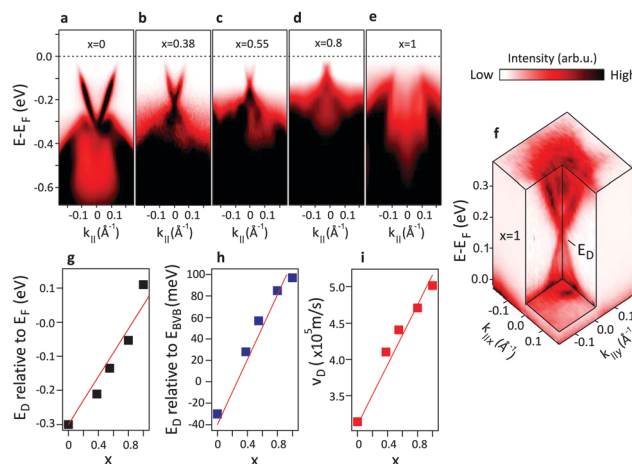Fig. 1 Clean surfaces of (Bi,Sb)$_2$Te$_3$: (a–e) The ARPES data for $(Bi_{1-x}Sb_x)_2Te_3$ of different composition obtained at a photon energy of 6 eV at 298 K; (f) the Dirac cone for clean Sb$_2$Te$_3$(111) obtained above the Fermi level following excitation by infrared fs-laser pulses. (g and h) The concentration dependence of the energy distance between (g) the Fermi level and the Dirac point, (h) the Dirac point and the top of the valence band and (i) the concentration dependence of the group velocity of Dirac fermions within the topological surface state.

The $(Bi_{1-x}Sb_x)_2Te_3$ film samples reported earlier behave differently.[27–30] For instance, for 8–56 nm thin films deposited on Si(111),[28] the ARPES data demonstrate that the FL is located within the bulk band gap for $x = 0.8$–0.9. At the same time, the transport measurements revealed low bulk carrier concentration for samples with $x = 0.40$–0.45. The authors attributed this discrepancy[28] to the fact that ARPES is a highly surface sensitive method, while electrical transport probes the entire system that can behave substantially different. There is general consistency between other data obtained for films grown by molecular beam epitaxy (MBE) on different substrates. Thuswise, for films grown on sapphire(0001) the insulating state was observed for $x = 0.95$ both by ARPES and Hall measurements.[27] For MBE films grown on highly doped Si(111) substrates,[29] the Dirac point was found to be within 10 meV around the Fermi level for $x = 0.94$. Besides, contributions from the bulk bands intersecting the Fermi level were not observed. For films on mica substrates a maximum of the sheet resistance was obtained for $x = 0.957$, indicating minimization of the bulk conductivity at this composition.[30] Besides, the authors[30] observed weak antilocalization with a coefficient of -0.43, which evidences the existence of two-dimensional (2D) surface states, and Shubnikov–de Hass oscillation behavior under high magnetic field. Finally, the 2D carrier density was found to be 0.81×10^{16} m^{-2}.

Despite the fact that for both our Bridgman crystals and the MBE films studied in ref. 27 the nutrient phase was enriched in Te, the truly bulk-insulating state appears at rather different x values. Most of the data obtained for MBE films reveal that low carrier concentration is realized near Sb_2Te_3 at $x = 0.9$–0.94, whereas for crystals grown from the Te-rich melt we observe the transition in the middle of the composition range, i.e. at $x = 0.55$–0.8. Although this seems contradictory at first sight, such behavior becomes less surprising when considering the phase diagram of the corresponding system. Generally, in case of quasibinary solid solutions $(A_{1-x}B_x)_{2-d}X_{3+d}$, the composition is characterized by the mole fraction x, which usually defines the energy band gap, and the deviation from stoichiometry d (i.e. the metal-to-chalcogen ratio), which influences the carrier concentration. For our system, there is a broad range of combinations of the mole fraction x and the deviation from stoichiometry d that ensures the insulating properties of the mixed crystals. For vapor growth all these combinations are potentially achievable, whereas the growth from the melt imposes certain constraints on them. In detail, the deviation from stoichiometry is controlled by the growth temperature (which is relatively high) and the melt composition. Thus, the solid composition lies at the solidus surface tracing around the homogeneity range of the mixed crystals in the equilibrium phase diagram. For a fixed value of the mole fraction x, the maximal solubility of Te depends strongly on the temperature. The films grow at much lower temperature (180 °C) than crystals (580–600 °C), therefore, d is different at a fixed x value.

To probe the chemical bonding in the mixed crystals we used XPS. The spectral shape for the Sb 4d, Bi 5d and Te 4d lines is described well by a single doublet each, which were assigned as the Sb I, Te I, Bi I components; an example is
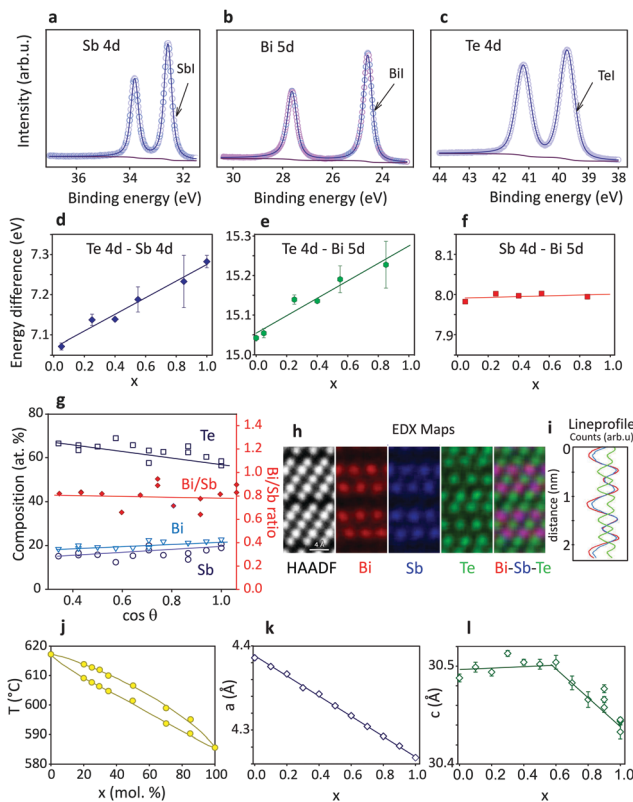

Fig. 2 Clean surfaces and cation distribution in $(Bi,Sb)_2Te_3$: (a–c) typical XP-spectra for clean (111). (d–f) Concentration dependence of the peak position difference for (d) Te 4d–Sb 4d, (e) Te 4d–Bi 5d, and (f) Bi 5d–Sb 4d. (g) Angular dependence of the composition for the crystals ($x = 0.55$) obtained by XPS at a kinetic energy of 100 eV. (h) A cross-sectional HAADF TEM image and compositional maps in counts for bulk crystal ($x = 0.55$) obtained by averaging different areas of multiple EDX maps with (i) the corresponding depth profile. (j) The equilibrium phase diagram of the quasibinary system Bi_2Te_3–Sb_2Te_3.[31] (k and l) Lattice constants (k) a and (l) c for the mixed crystals.

shown in Fig. 2a–c. Therefore, all atoms of the same element are equivalent to each other with respect to the electron density. The peak positions are close to those of clean Bi_2Te_3 and Sb_2Te_3, correspondingly. More precisely, the difference in binding energies (BEs) between the Te 4d and Sb 4d peaks (Fig. 2d), as well as between the Te 4d and Bi 5d ones (Fig. 2e) increases linearly by ~ 0.3 eV depending on the mole fraction x, which indicates an upshift of Te 4d (lower negative charge for higher x) and/or a downshift of Sb 4d and Bi 5d (lower positive charge for higher x). One can note that the difference in the cation-related peak positions does not depend on the composition of the solid solution (Fig. 2f) due to an even distribution of the positive charge between the cations for all compositions. All these observations suggest gradual decrease of the averaged charge transfer from the metal to Te (i.e. the bond ionicity) for the mixed crystals with a higher Sb_2Te_3 content. Such behavior indicates the substitutional nature of the solid solutions and the ideal mixing with no ordering in the cation sublattice.

It should be noted that ordering is typical for anion substitution in tetradymite phases like the $Bi_2(Se_{1-x}Te_x)_3$ mixed

crystals, which yield well-defined individual layers of Se and Te and give, for instance, an ordered phase of Bi_2SeTe_2 (1 quintuple layer (QL) = Te–Bi–Se–Bi–Te). Potentially, ordering can also exist for $(Bi,Sb)_2Te_3$ near $x = 0.5$ that gives the Te–Sb–Te–Bi–Te layers. If the ordering takes place, the surface or the second atomic layer may be preferentially composed of Sb or Bi. As Sb_2Te_3 is much more reactive than Bi_2Te_3, this kind of ordering strongly influences the surface reactivity especially at the early stages. However, the cross-sectional HAADF STEM image combined with the atomic resolution EDX maps shown in Fig. 2h evidence that both Sb and Bi are evenly distributed in the crystal bulk. In addition, to check whether the second layer is preferentially occupied by Sb or Bi, we have studied the angular dependence of the surface composition obtained from the photoemission data for an electron kinetic energy (KE) of 100 eV, which provides the ultimate surface sensitivity. An example is presented in Fig. 2g. Naturally, the Te concentration increases for the shallow angles, whereas the Bi to Sb ratio remains constant. Therefore, the cations are statistically distributed showing no surface enrichment either in Sb or Bi. Note that no ordering is expected based on the Bi_2Te_3–Sb_2Te_3 equilibrium phase diagram shown in Fig. 2j, which is close to that of ideal solid solutions.[31] In addition, as shown in Fig. 2k, the in-plane lattice constant a is a linear function of the mole fraction (a, $A = 4.3876(8)–0.120(1)x$) and obeys the Vegard's law typical for the ideal mixing. In the perpendicular direction, on the other hand, the lattice

constant c is only slightly different for the constituent phases (see Fig. 2l) and its minor variation is non-linear since the layer thickness is mostly influenced by the larger cations.

Oxidation

Oxide layer composition and interface structure. A typical example of high resolution core level spectra for the oxidized surface of the $(Bi,Sb)_2Te_3$ mixed crystals is presented in Fig. 3a–c, and the corresponding spectral features are summarized in Table 1. Compared to the clean surface, the Sb 4d spectra for all sample compositions attain an additional component Sb II upon oxidation, which is split from the initial component by 1.6 eV and corresponds to the Sb–O–Te bonds.[1] The angular dependence of the relative intensities from the Sb I and Sb II components presented in Fig. 3e indicates the surface location of the atoms related to the Sb II component. All Bi 5d spectra can also be described well by two components, with the new feature Bi II appearing at a higher binding energy with a chemical shift of 1.6 eV, which we assign to the Bi–O bonds. The surface location of the atoms associated with the Bi II component is clearly seen in Fig. 3f. The Te 4d spectra, on the other hand, have a complex structure and are composed of three additional components with chemicals shifts of 0.6 eV (Te II), 1.1 eV (Te III) and 3.9 eV (Te IV), with the latter corresponding to the Te^{4+} formal oxidation state (Fig. 3d). All in all, the spectra can be well described by a proper combination
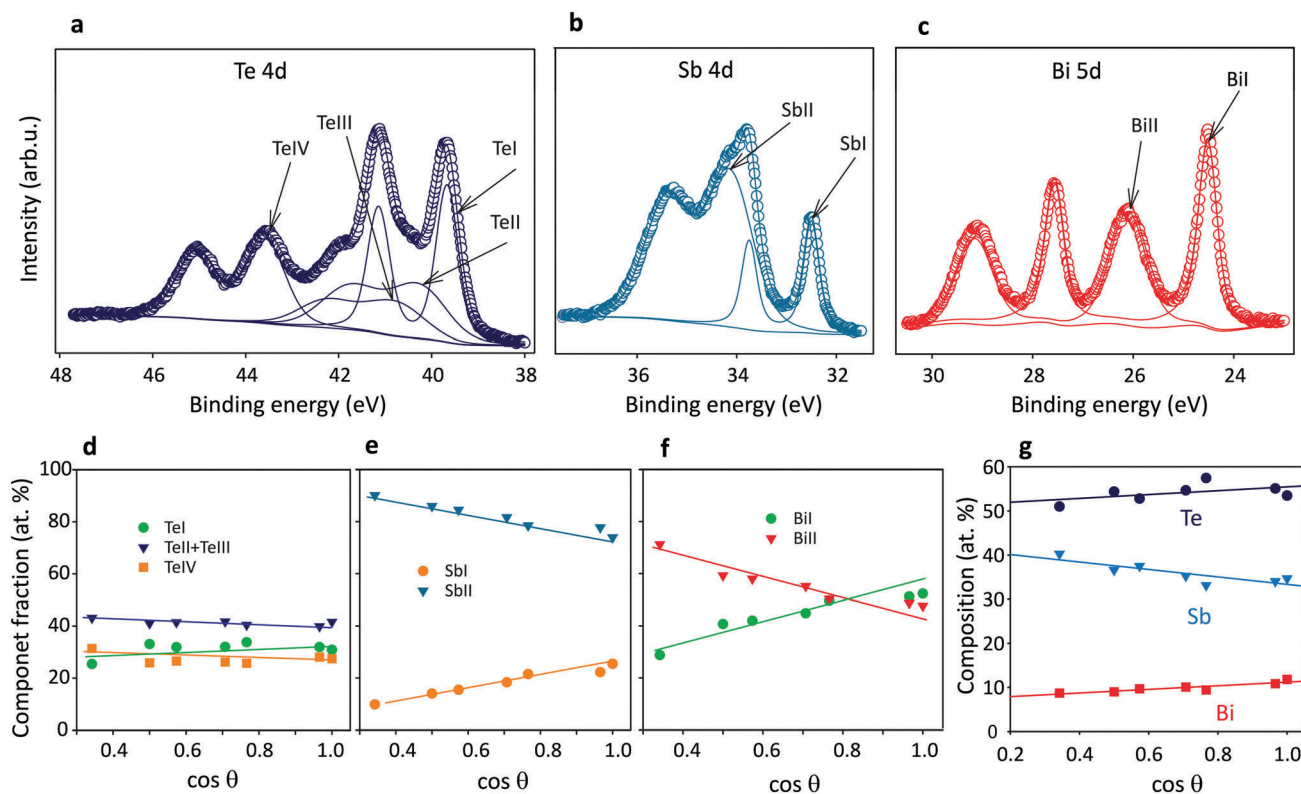

Fig. 3 Photoemission data for the oxidized surface of $(Bi,Sb)_2Te_3$. $x = 0.85$, KE = 100 eV: (a–c) typical spectra measured *ex situ*, (d–f) angular dependencies of the corresponding spectral components, θ is the angle between the emitted electrons and the surface normal. (g) Angular dependence of the surface composition.

8944 | *J. Mater. Chem. C*, 2018, **6**, 8941–8949

This journal is © The Royal Society of Chemistry 2018

Table 1 Te 4d, Sb 4d and Bi 5d spectral features for the oxidized surfaces (units are in eV)

	Te I	Te II	Te III	Te IV	Sb I	Sb II	Bi I	Bi II
Ex situ data								
$(Bi,Sb)_2Te_3$	0	0.6	1.1	3.9	0	1.6	0	1.6
Bi_2Te_3	0	—	1.3	3.8			0	1.5
Sb_2Te_3	0	0.6	1.1	3.9	0	1.6		
In situ data								
$(Bi,Sb)_2Te_3$	0	0.7	1.2	3.9	0	1.65	0	1.6
Bi_2Te_3	0	0.8	1.3	3.8			0	1.4
Sb_2Te_3	0	0.6	1.1	3.8	0	1.6		

of the components from the oxidized surfaces of Sb_2Te_3[1] and Bi_2Te_3[2] as it follows from the data in Table 1.

The angular dependence of the surface composition in Fig. 3g indicates notable surface enrichment in antimony evidencing high Sb concentration in the oxide layer. To get further insight into the oxidation mechanism, we used HAADF STEM and STEM-EDX mapping. In Fig. 4a one can clearly see that the oxide layer covers the whole surface after two months ($\sim$1500 h) of air exposure. It is amorphous, and its surface is somewhat rough. The oxide-crystal interface is sharp (for more details, see ESI†).

The oxide layer (*i.e.* the layer where oxygen is present) has a non-uniform in-depth component distribution. The EDX maps taken with atomic resolution and the corresponding composition profiles (Fig. 4a) clearly indicate that the upper part of the oxide layer is composed of antimony oxide (region 0), whereas strong depletion of Sb from the first QLs of the crystal is observed (regions 1 and 2). Besides, this layer contains a certain amount of oxygen. At the same time, the Bi density slightly increases and the Te density is the same as in the bulk. This indicates generation of Sb vacancies in the surface layer of the crystal. The crystal structure remains intact in this case. However, prolonged oxidation (about 3 years) results in certain structural changes. The corresponding TEM data are presented in Fig. 4b. By comparing these two datasets we conclude that although the thickness of the amorphous layer practically does not change, certain Te redistribution is observed. The Te density becomes higher for the amorphous layer/crystal interface. Besides, the subsurface layer is strongly distorted and has a significant amount of defects like the septuple layers marked by white arrows in Fig. 4b. The septuple layers have a higher cation to anion ratio of atomic positions, hence many cation positions are vacant, which enables atomic mobility. In addition, the XPS data
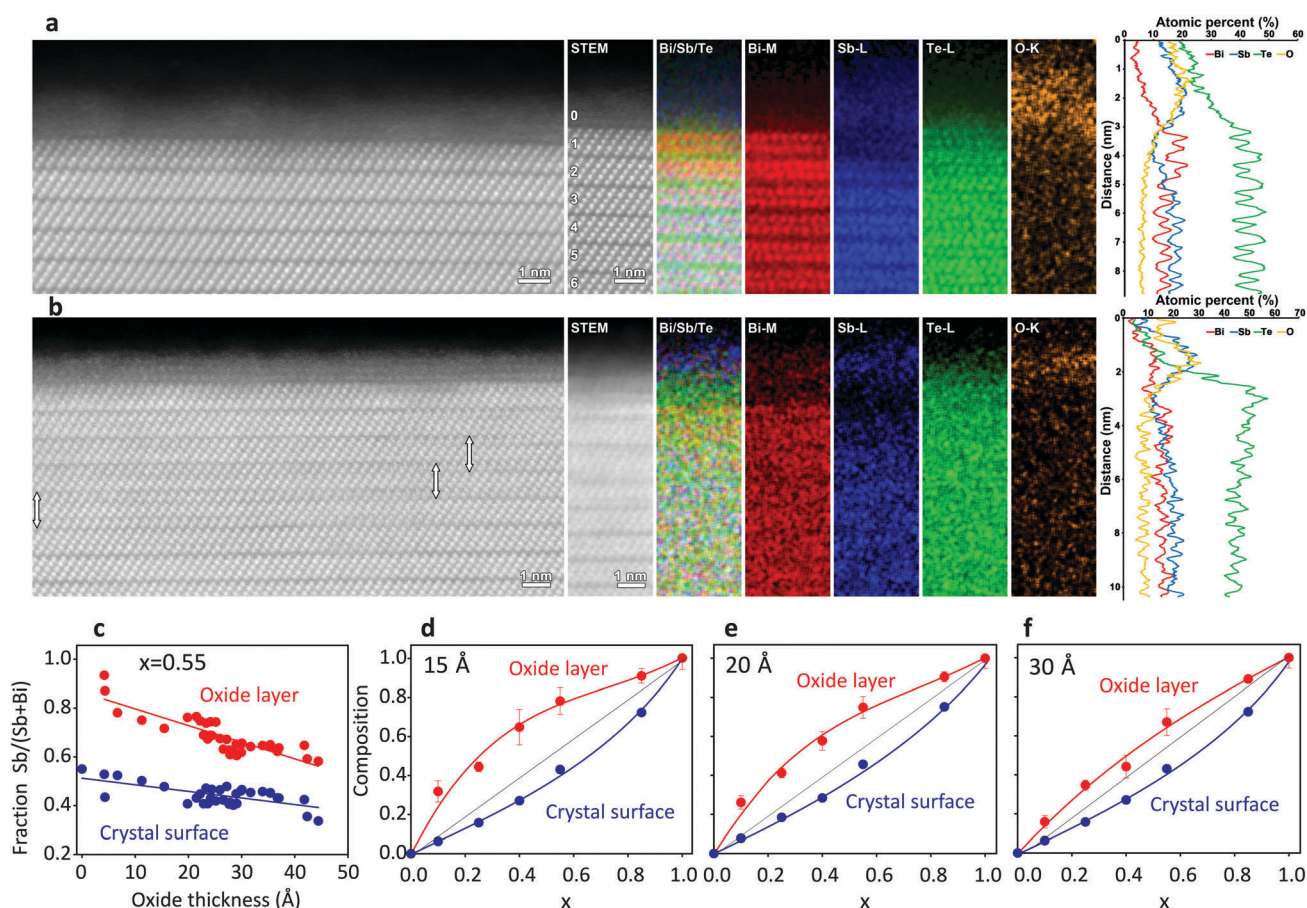

Fig. 4 The oxide layer composition and the interface structure. (a) From left to right, a cross-sectional image for the $(Sb_{0.55}Bi_{0.45})_2Te_3$ crystal (111) surface layer, element-resolved EDX maps, and composition (in counts) as a function of depth after 2 months of oxidation. (b) Similar results as in (a) after 3 years of oxidation. (c) Thickness dependence of the oxide layer composition (*ex situ* data, Al Kα). (d–f) The oxide layer and the crystal surface composition as a function of x for 3 different values of the oxide layer thickness.

indicate that in the course of oxidation, the composition of both the oxide layer and the crystal surface layer varies. An example is provided in Fig. 4c where the dependence of the oxide and crystal surface compositions on the thickness of the oxide layer is demonstrated. These compositions are calculated from the corresponding intensities of the oxide-related spectral features (Bi II, Sb II, Te II–IV) and the features related to the clean crystal surface (Bi I, Sb I, Te I) in the XPS data. In the beginning, the oxide layer is strongly enriched in antimony. The Sb concentration further decreases both in the oxide layer and in the surface layer of the crystal, most probably due to slow solid state diffusion. Note that the relative enrichment of the oxide layer and depletion of Sb from the crystal surface does not depend on the initial crystal composition x in the range of $x = 0.1$–0.6. For higher x values the depletion of Sb is lower. This is illustrated in Fig. 4d–f for three different thickness values.

To interpret these observations, we should take into account that the constituents Bi_2Te_3 and Sb_2Te_3 exhibit radically different oxidation behavior. In the case of bismuth telluride, the Bi to Te ratio in the oxide layer is the same as in the bulk crystal.[2] We suppose that the oxidation reaction occurs at the oxide–crystal interface, and oxygen diffusion into the oxide layer is part of the oxidation mechanism. The oxide layer at the antimony telluride surface is enriched in Sb and corresponds to the $Sb_2Te_2O_7$ stoichiometry.[1] Here, therefore, on the contrary, Sb diffuses towards the oxide surface. Besides, the oxidation of Sb_2Te_3 proceeds much faster. The same situation is observed also for PbTe[4] as compared to SnTe[5] or GeTe.[6] In the oxide layer of the mixed crystals we observe strong redistribution of Sb and Bi between the oxide layer and the crystal surface due to fast Sb diffusion caused by the strong affinity of Sb to oxygen, $i.e.$ by the fact that the Sb–O bond is much stronger than the Bi–O and Te–O bonds. The corresponding formation energy $(-H_f^\circ)$ for Sb_2O_3 is 715 kJ mole^{-1}, for Bi_2O_3 it is 565 kJ mole^{-1}, while for TeO_2 it comprises 322 kJ mole^{-1}.[32]

Oxidation kinetics

Significant scattering of the experimental points in Fig. 5 is typical for Sb_2Te_3[1] as well as for the mixed crystals. We find that different parts of the same sample show different results, thus the scattering is not due to the surface preparation (some random unremoved pre-oxidized areas) or an effect of uncontrolled humidity. The scattering can be explained by the combination of a slow first step and a very fast second step as follows. As the induction period is of statistical nature (from minutes to hours), and it is followed by fast oxidation of the first QL, it is their combination that gives rise to the scattering. One can assume that surface defects like terraces might play a role in lowering the activation energy for the first step. Since the density of steps at the surface is very low at the surface, the oxidation threshold can be expected to be highly sensitive to variations in the surface defect density. The behavior of the mixed crystals in this sense is similar to that of Sb_2Te_3.

The third step – the oxide layer growth – requires diffusion of either oxygen to the interface or of crystal components through the oxide layer to the surface. The oxidation rate is also dependent on the structure of the oxide layer, as well as on the presence of
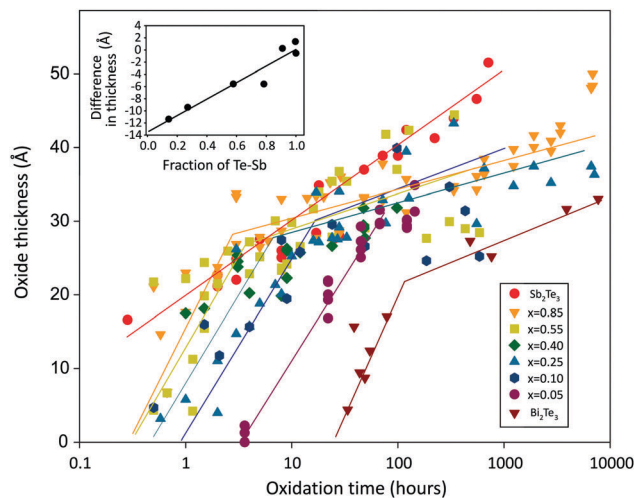

Fig. 5 The oxidation kinetics studied by ex $situ$ XPS. The oxide layer thickness for the (111) surfaces of $(Sb_xBi_{1-x})_2Te_3$ crystals of different composition in humid air (humidity 44%, 298 K) calculated from the Te 3d spectra measured using the Al K_α emission. Inset: Surface reactivity expressed by the averaged difference in the oxide thickness between the Sb_2Te_3 and $(Bi_{1-x}Sb_x)_2Te_3$ crystals $vs.$ fraction of the surface Te atoms bonded to at least one Sb atom.

any pores or cracks. At the third step, we observe that the oxide layer composition, while strongly enriched in Sb compared to the crystal bulk at the beginning of oxidation, changes in time (Fig. 5). The enrichment tends to decrease due faster variation of the composition in the oxide layer than at the crystal surface. When the oxide layer thickness is about 3 nm its growth rate decreases in most of the cases; thus, there is a tendency to surface passivation for the mixed crystals in contrast to Sb_2Te_3.

Let us now discuss comparative reactivity of the mixed crystals as a function of x and its correlation with that of Bi_2Te_3 and Sb_2Te_3. Taking into account the data scattering we propose the following approach. To characterize the reactivity we take as a benchmark the mean deviation of the experimental points (in thickness) from the line obtained for the most reactive constituent (Sb_2Te_3 in the range of 0–3 nm). These values are found to be in poor correlation with x as it is shown in Fig. S6a of the ESI.† To find a better descriptor we assumed that the Te–M bonds (M = Bi,Sb) are attacked by oxygen since the clean surface of all samples is terminated by Te, with this process having the highest energy barrier in the oxidation mechanism. Therefore, one can conclude that the reactivity is proportional to the fraction of the Te atoms bonded to at least a single Sb atom. This dependence is shown in the inset of Fig. 5. As we can see, there is a linear correlation of the reactivity with the proposed descriptor. This observation also implies a decisive role of the first step, $i.e.$ oxygen attack on the Te–Sb bonds, in the oxidation behavior of the solid solutions based on Sb_2Te_3. All in all, the surface reactivity of the mixed crystals depends on their composition, but it is not a linear combination of the values from their constituents. The concentration effect is much more pronounced for low x values. For $x > 0.5$, on the other hand, the reactivity does not differ from that of Sb_2Te_3.

It should be noted that the *ex situ* XPS analysis commonly used to probe the surface reactivity has certain limitations since it assumes, for instance, that the reaction products remain unmodified when the sample is evacuated after the gas exposure. Therefore, it is not a truly kinetic experiment, in addition to the fact that some processes potentially can take place after the exposure like decomposition of short-living species. The question arises whether the data obtained *ex situ* are relevant to the oxidation kinetics. To resolve this issue, advanced methods for *in situ* studies have been developed recently, with near-ambient pressure (NAP XPS) being the most promising among them.[33] However, this method has been applied mostly in catalysis and, to the best of our knowledge, no semiconductor crystal reactivity studies have been undertaken so far. We have utilized this approach to trace the oxidation mechanism for the mixed crystals in more detail, especially at the early stages.

The results are illustrated in Fig. 6. The data for the mixed crystals clearly fall between those for their constituents (Fig. 6i). In all experiments the oxidation started without any measurable delay, therefore the induction period is negligible due to the oxygen activation by photons. Besides, the oxidation rate is generally much higher than for the *ex situ* experiments.
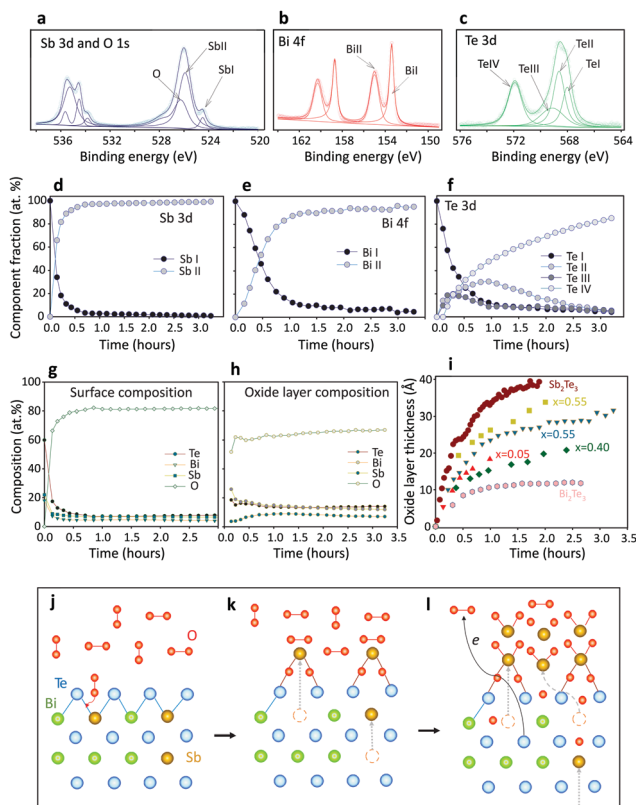
Typical spectra obtained during *in situ* oxidation are presented in Fig. 6a–c. They can be treated with the same set of spectral components as we used for the *ex situ* experiments, and we conclude, therefore, that the oxidation related species are rather similar and that the *ex situ* studies are relevant for our discussion.

The behavior of the spectral components in Fig. 6d–f suggests that the process starts with antimony oxidation, which quickly reaches saturation already after 0.5 h together with the surface concentration of oxygen (Fig. 6g and h). This point corresponds to the maximal intensity of the Te III component, which is an intermediate. Moreover, the surface is enriched in Sb. We assume that at this stage oxygen attacks the Te–Sb bonds at the surface and thereby becomes bonded to both Sb and Te and gives rise to the Sb II and Te III spectral features.

The underlying mechanism responsible for this behavior is schematically shown in Fig. 6j–l. First, the Te–Bi bonds are attacked by molecular oxygen (Fig. 6j). Once the surface Te–Sb bonds are saturated with oxygen (Fig. 6k), the other Sb atoms migrate to the surface to form an antimony oxide layer and leave cation vacancies in two QLs of the crystal according to the TEM data. How many Sb vacancies can be formed without any lattice destruction? The XRD data in Fig. 2l showing the change in the lattice constant c as a function of x give us a hint: up to 50% Sb substitution the lattice constant does not change, hence the lattice is stable due to the larger Bi atoms. As a consequence, up to 50% cation vacancies can be formed. We suppose that the antimony layer forms due to Sb diffusion as the initial part of the kinetic curves in Fig. 6i for the whole composition range is linearized with respect to the diffusion coordinates $t^{1/2}$. The driving force for such behavior is the formation of strong Sb–O bonds. At the next step, all available Sb atoms migrate and oxidize (Fig. 6l), and the observed behavior has some similarity with the Cabrera–Mott mechanism.[34] This means that oxygen adsorbed at the surface attains electrons from the Fermi level of the crystal by tunneling through the Sb_2O_3 layer. As the Te–Bi hybrid p orbitals mostly contribute to the density of states at the Fermi level, Te becomes more "oxidized" due to the electron transfer that gives rise to the Te II component, which does not correspond to Te bonded to O due to a small chemical shift. Its maximal intensity also corresponds to the complete oxidation of the surface Bi atoms. The oxygen ions can diffuse through the oxide layer, finally converting Te to the +4 oxidation state until the oxide layer becomes too thick for further tunneling. After prolonged exposures, Te accumulates at the interface and causes a lattice disturbance in the form of septuple layer defects (Fig. 4b).

Our *in situ* measurements also demonstrate that to evaluate the overall reactivity the first oxidation step is of most importance. Our NAP XPS measurements show that oxygen is activated by the photon beam and that the barrier for oxidation reaction at the surface can be easily overcome. In this case, the oxidation rate depends on the composition only slightly. In particular, the oxidation rate is mostly determined by inert impurities like CO, CO_2 and H_2O that adsorb and block the availability of the surface adsorption sites for oxygen.[1]

Fig. 6 The oxidation kinetics for the $(Bi_{1-x}Sb_x)_2Te_3$ crystal (111) surface (*in situ* data, $T = 298$ K, $p(O_2) = 0.5$ mbar, the electron energy is 200 eV): (a–c) the XP spectra of the Sb 3d + O 1s, Te 3d, Bi 4f lines; (d–f) time dependencies of the spectral components for the Sb 3d, Bi 4f, Te 3d spectra; (g) time dependence of the surface composition, (h) time dependence of the oxide layer composition, (i) oxidation kinetics for different compositions. (j–l) A schematic presentation of the reaction mechanism.

The main text of the article should appear here with headings as appropriate.

Experimental

$(Bi,Sb)_2Te_3$ single crystals were grown from the melt by the Bridgman method using a similar procedure to that described in detail for $(Pb,Sn)Se$.[35] More precisely, the solidification time of the crystals was 1 week, and the pulling rate was 0.2 mm h^{-1}. The temperature gradient during growth was 5 °C cm^{-1} and growth temperatures were in the range of 580–600 °C. Other details are presented in SI file (part 1) (ESI†).

Crystals were cleaved *in situ* for ARPES and near ambient pressure (NAP) core-level X-ray photoemission (XPS) experiments or *ex situ* for photoemission studies of oxidation at high exposures. The high quality of the (111) surfaces was verified by low-energy electron diffraction (LEED) and by the presence of sharp features in the ARPES dispersions. For the *ex situ* oxidation experiments, freshly cleaved surfaces were exposed for certain periods of time to air at 1 bar pressure, 23 ± 2 °C temperature and humidity of 44%.

The ARPES experiments were performed at room temperature using the first (1.5 eV) and the fourth (6 eV) harmonics of a homemade fs-laser system coupled with an ultrafast amplifier operating at a 100 kHz repetition rate. Photoelectrons were detected with a Scienta R4000 hemispherical analyzer, and the angular and energy resolutions were 0.2° and 30 meV, respectively.

The core-level photoemission studies were carried out using several facilities of Helmholtz-Zentrum Berlin, Germany, and ALBA Synchrotron Light Source in Barcelona, Spain. The Bi 5d, Sb 4d, Te 4d and O 1s spectra were recorded with high surface sensitivity at the Russian-German beamline using the photoelectron kinetic energies of 50 and 100 eV. The XPS spectra acquisition was performed using a SPECS Phoibos 150 electron energy analyzer at variable detection angles. The NAP XPS data were obtained at the ISISS and CIRCE beamlines equipped with a SPECS Phoibos 150 NAP analyzer under the oxygen pressures of 0.5 mbar. The Sb 3d, Te 3d, Bi 4f and O 1s spectra were recorded at an electron kinetic energy of 200 eV. We used kinetic energy of 200 eV for *in situ* NAP XPS to study the reaction mechanism at the same depth from the sample surface. The latter is important to find quantitative correlation between the spectral components related to different elements. Also important is that 200 eV corresponds to the minimal energy at which Yeh-Lindau theoretical cross-sections work.

The long-term oxidation kinetics was studied using a Kratos Axis Ultra laboratory system equipped with a monochromatic Al K$_\alpha$ X-ray source. All XPS spectra were fitted by Gaussian/Lorentzian convolution functions with simultaneous optimization of the background parameters using Unifit 2014 computer program. The background was modeled using a combination of Shirley- and Tougaard-like backgrounds. One should note that the probing depth for Sb and Te are very similar (corresponds to kinetic energy of around 1000 eV), and only for Bi 4f it is higher. This have been taken into account in the data analysis.

For high-angle annular dark-field scanning transmission electron microscopy (HAADF-STEM) imaging and energy dispersive X-ray (EDX) mapping, cross sectional samples were prepared on a Cu support by focused ion beam (FIB) milling. A carbon layer was deposited onto the material to protect it from damage during the preparation. The HAADF-STEM and EDX data were acquired on an aberration-corrected FEI Titan transmission electron microscope operating at 200 kV, equipped with a Super-X detector.

Conclusions

The oxidation process of the quasibinary solid solutions is rather complex. With the example of $(Bi,Sb)_2Te_3$ mixed crystals we developed a phenomenological model of their reaction with molecular oxygen. The reactivity of the mixed crystals is not a linear combination of the reactivity of its constituents. In the case of tetradymite compounds it is more influenced by the higher reactive constituent. We found a proper descriptor for the experimental observations. We revealed that the surface reactivity is proportional to the number of the Te atoms bonded to at least one Sb atom, and therefore, it is determined by the probability of oxygen attack on the Te–Sb bonds. The oxidation process includes the growth of a dense and amorphous antimony oxide layer due to Sb diffusion from the first two quintuple layers to the surface, as it follows from the atomically resolved TEM/EDX experiments. This process also involves electron tunneling to oxygen through the oxide layer, oxygen ion diffusion to the crystal surface, and, finally, slow Te oxidation to a +4 oxidation state. The oxide layer thickness is limited by the electron tunnelling threshold for the growing insulating oxide layer. Comparison of the data obtained by *ex situ* and *in situ* measurements in the oxygen atmosphere reveals that oxygen activation is induced by the photon beam, an effect that substantially reduces the induction period, whereas the main stages of the oxidation mechanism remain unchanged. Therefore, our observations confirm that the combination of NAP XPS recorded at the same kinetic energy for all elements with cross-sectional atomic resolution TEM/EDX is a powerful tool to probe the surface chemistry of semiconductor materials and topological insulators.

Author contributions

Andrey A. Volykhov, Anna P. Sirotina and Lada V. Yashina carried out XPS data treatment and interpretation. Anna P. Sirotina, Vera S. Neudachina, Alina I. Belova, Nikolay O. Khmelevsky, Carlos Escudero, Virginia Pérez-Dieste, Axel Knop-Gericke and Lada V. Yashina organised and performed XPS experiments. Jaime Sánchez-Barriga performed ARPES studies. Maria Batuk, Carolien Callaert and Joke Hadermann conducted TEM studies. Nadezhda V. Vladimirova, Marina E. Tamm did experiments on crystal growth and characterization. Lada V. Yashina conceived and coordinated the project. Lada V. Yashina and Jaime Sánchez-Barriga wrote the manuscript with input from all authors.

Conflicts of interest

The authors declare no competing financial interest.

8948 | *J. Mater. Chem. C*, 2018, **6**, 8941–8949

This journal is © The Royal Society of Chemistry 2018

Acknowledgements

Notes and references

1 A. A. Volykhov, J. Sánchez-Barriga, A. Sirotina, V. Neudachina, A. Frolov, E. Gerber, E. Kataev, B. Senkovskiy, N. Khmelevsky, A. Aksenenko, N. Korobova, A. Knop-Gericke, O. Rader and L. V. Yashina, *Chem. Mater.*, 2016, **28**, 8916.

2 L. V. Yashina, J. Sánchez-Barriga, M. Scholz, A. A. Volykhov, A. Sirotina, V. Neudachina, M. Tamm, A. Varykhalov, D. Marchenko, G. Springholz, G. Bauer, A. Knop-Gericke and O. Rader, *ACS Nano*, 2013, **7**, 5181.

3 A. A. Volykhov, L. V. Yashina, T. S. Zyubina, V. I. Shtanov, V. N. Neudachina, R. Püttner and A. S. Zyubin, *Russ. J. Inorg. Chem.*, 2011, **56**, 1284.

4 L. V. Yashina, T. S. Zyubina, R. Püttner, A. S. Zyubin, V. I. Shtanov and A. E. Tikhonov, *J. Phys. Chem. C*, 2008, **112**, 19995.

5 V. S. Neudachina, T. B. Shatalova, V. I. Shtanov, L. V. Yashina, T. S. Zyubina, M. E. Tamm and S. P. Kobeleva, *Surf. Sci.*, 2005, **584**, 77.

6 L. V. Yashina, R. Püttner, V. S. Neudachina, T. S. Zyubina, V. I. Shtanov and M. V. Poygin, *J. Appl. Phys.*, 2008, **103**, 094909.

7 R. Schennach, S. Promreuk, D. G. Naugle and D. L. Cocke, *Oxid. Met.*, 2001, **55**, 523.

8 M. Z. Hasan and C. L. Kane, Colloquium: topological insulators, *Rev. Mod. Phys.*, 2010, **82**, 3045.

9 X.-L. Qi and S.-C. Zhang, *Rev. Mod. Phys.*, 2011, **83**, 1057.

10 Y. L. Chen, J. G. Analytis, J.-H. Chu, Z. K. Liu, S.-K. Mo, X. L. Qi, H. J. Zhang, D. H. Lu, X. Dai, Z. Fang, S. C. Zhang, I. R. Fisher, Z. Hussain and Z.-X. Shen, *Science*, 2009, **325**, 178.

11 D. Hsieh, Y. Xia, L. Wray, D. Qian, A. Pal1, J. H. Dil, J. Osterwalder, F. Meier, G. Bihlmayer, C. L. Kane, Y. S. Hor, R. J. Cava and M. Z. Hasan, *Science*, 2009, **323**, 919.

12 D. Hsieh, Y. Xia, D. Qian, L. Wray, F. Meier, J. H. Dil, J. Osterwalder, L. Patthey, A. V. Fedorov, H. Lin, A. Bansil, D. Grauer, Y. S. Hor, R. J. Cava and M. Z. Hasan, *Phys. Rev. Lett.*, 2009, **103**, 146401.

13 R. Yoshimi, A. Tsukazaki, Y. Kozuka, J. Falson, K. S. Takahashi, J. G. Checkelsky, N. Nagaosa, M. Kawasaki and Y. Tokura, *Nat. Commun.*, 2015, **6**, 6627.

14 L. Fu, *Phys. Rev. Lett.*, 2009, **103**, 266801.

15 J. Sánchez-Barriga, A. Varykhalov, J. Braun, S.-Y. Xu, N. Alidoust, O. Kornilov, J. Minár, K. Hummer, G. Springholz, G. Bauer, R. Schumann, L. V. Yashina, H. Ebert, M. Z. Hasan and O. Rader, *Phys. Rev. X*, 2014, **4**, 011046.

16 L.-L. Wang, M. Huang, S. Thimmaiah, A. Alam, S. L. Bud'ko, A. Kaminski, T. A. Lograsso, P. Canfield and D. D. Johnson, *Phys. Rev. B: Condens. Matter Mater. Phys.*, 2013, **87**, 125303.

17 K. A. Kokh, S. V. Makarenko, V. A. Golyashov, O. A. Shegaid and O. E. Tereshchenko, *CrystEngComm*, 2014, **16**, 581.

18 S. Jia, H. Ji, E. Climent-Pascual, M. K. Fuccillo, M. K. Charles, J. Xiong, N. P. Ong and R. J. Cava, *Phys. Rev. B: Condens. Matter Mater. Phys.*, 2011, **84**, 235206.

19 M. S. Bahramy, P. D. King, A. de la Torre, J. Chang, M. Shi, L. Patthey, G. Balakrishnan, P. Hofmann, R. Arita, N. Nagaosa and F. Baumberger, *Nat. Commun.*, 2012, **3**, 1159.

20 Z. Ren, A. A. Taskin, S. Sasaki, K. Segawa and Y. Ando, *Phys. Rev. B: Condens. Matter Mater. Phys.*, 2010, **82**, 241306(R).

21 B. Xia, P. Ren, A. Sulaev, P. Liu, S.-Q. Shen and L. Wang, *Phys. Rev. B: Condens. Matter Mater. Phys.*, 2013, **87**, 085442.

22 C. Niu, Y. Dai, Y. Zhu, Y. Ma, L. Yu, S. Han and B. Huang, *Sci. Rep.*, 2012, **2**, 976.

23 S. Jia, H. Beidenkopf, I. Drozdov, M. K. Fuccillo, J. Seo, J. Xiong, N. P. Ong, A. Yazdani and R. J. Cava, *Phys. Rev. B: Condens. Matter Mater. Phys.*, 2012, **86**, 165119.

24 Z. Ren, A. A. Taskin, S. Sasaki, K. Segawa and Y. Ando, *Phys. Rev. B: Condens. Matter Mater. Phys.*, 2010, **82**, 241306(R).

25 K. Miyamoto, A. Kimura, T. Okuda, H. Miyahara, K. Kuroda, H. Namatame, M. Taniguchi, S. V. Eremeev, T. V. Menshchikova, E. V. Chulkov, K. A. Kokh and O. E. Tereshechenko, *Phys. Rev. Lett.*, 2012, **109**, 166802.

26 T. Knispel, W. Jolie, N. Borgwardt, J. Lux, Z. Wang, Y. Ando, A. Rosch, T. Michely and M. Grüninger, *Phys. Rev. B*, 2017, **96**, 195135.

27 J. Zhang, C.-Z. Chang, Z. Zhang, J. Wen, X. Feng, K. Li, M. Liu, K. He, L. Wang, X. Chen, Q.-K. Xue, X. Ma and Y. Wang, *Nat. Commun.*, 2011, **2**, 574.

28 C. Weyrich, M. Drögeler, M. Kampmeier, M. Eschbach, G. Mussler, T. Merzenich, T. Stoica, I. E. Batov, I. E. Schubert, L. Plucinski, B. Beschoten, C. M. Schneider, C. Stampfer, D. Grützmacher and Th. Schäpers, *J. Phys.: Condens. Matter*, 2016, **28**, 495501.

29 J. Kellner, M. Eschbach, J. Kampmeier, M. Lanius, E. Młyńczak, G. Mussler, B. Holländer, L. Plucinski, M. Liebmann, D. Grützmacher, C. M. Schneider and M. Morgenstern, *Appl. Phys. Lett.*, 2015, **107**, 251603.

30 Y. Ni, Z. Zhang, C. I. Nlebedim and D. C. Jiles, *AIP Adv.*, 2016, **6**, 055812.

31 T. Caillat, M. Carle, D. Perrin, H. Scherrer and S. Scherrer, *J. Phys. Chem. Solids*, 1992, **53**, 227.

32 Database "Thermodynamic constants of substances"? show= welcome.html&_ga=2.174006947.1428104881.1519653884-172022318.1455030626.

33 M. Salmeron and R. Schlögl, *Surf. Sci. Rep.*, 2008, **63**, 169.

34 N. Cabrera and N. F. Mott, *Rep. Prog. Phys.*, 1949, **12**, 163.

35 V. I. Shtanov and L. V. Yashina, *J. Cryst. Growth*, 2009, **311**, 3257.

This journal is © The Royal Society of Chemistry 2018

J. Mater. Chem. C, 2018, **6**, 8941–8949 | 8949